Soft Matter

PAPER

View Article Online
View Journal | View Issue

Cite this: *Soft Matter*, 2019, **15**, 2638

Equilibrium configurations and capillary interactions of Janus dumbbells and spherocylinders at fluid–fluid interfaces†

Carmine Anzivino,[a] Fuqiang Chang,[b] Giuseppe Soligno,[c] René van Roij,[d] Willem K. Kegel[b] and Marjolein Dijkstra *[a]

Received 20th November 2018,
Accepted 25th February 2019

DOI: 10.1039/c8sm02361a

rsc.li/soft-matter-journal

We numerically investigate the adsorption of a variety of Janus particles (dumbbells, elongated dumbbells and spherocylinders) at a fluid–fluid interface by using a numerical method that takes into account the interfacial deformations. We first determine the equilibrium configuration of a single adsorbed particle, and we find that the overall shape of the induced deformation field has a strong hexapolar mode while non-Janus particles of the same shape do not induce any interfacial deformation. We then calculate the capillary interactions between two Janus spherocylinders adsorbed at an interface. The hexapolar deformation field induces capillary attractions for laterally aligned Janus spherocylinders and repulsions for laterally anti-aligned ones. We also experimentally synthesize micrometer-sized charged Janus dumbbells and let them adsorb at a water–decane interface. After several hours we observe the formation of aggregates of dumbbells predominantly induced by interactions that appear to be capillary in nature. Our Janus dumbbells attach laterally and are all aligned, as predicted by our numerical calculations.

I. Introduction

Colloidal particles with dimensions between 1 nm and 1 μm strongly adsorb at a fluid–fluid interface and can self-assemble into 2D ordered structures.[1–3] The adsorption of colloids is a well understood phenomenon: the interfacial area and hence the free energy of the interface can be reduced by the adsorption of particles at the interface.[4] By contrast, the self-assembly process is still not well understood even though a well-known, macroscopic analogue exists in everyday life when mm–cm sized breakfast cereals cluster in a bowl of milk. In the case of this so-called Cheerios effect[5] the gravitational force pulls the cereals down causing deformations in the fluid interface that are in turn responsible for capillary attractions among the cereals and consequently for the self-assembly process. As the gravitational effects can be neglected in the case of colloidal particles,[6–8] the colloidal self-assembly at a fluid–fluid interface arises from a more intricate phenomenon, although capillarity still plays an important role as we will see. The self-assembly of colloids trapped at a fluid–fluid interface can only be explained by forces that are sufficiently long-ranged and extend over distances many times the particle dimension.[9] Hence, the colloidal self-assembly cannot be explained by electrostatic and van der Waals forces[10] as these are not sufficiently long-ranged in most solvents. However, interfacial deformations are long-ranged. The interfacial deformations arising by sub-mm particles are induced by particle properties such as the shape and the surface chemistry rather than by gravitational effects.[11–19] The behavior of particles with homogeneous chemical properties but anisotropic shape, *e.g.* rods, cylinders, cubes, dumbbells and discs, at fluid–fluid interfaces has been widely studied.[20–23] Since the combined effect of the anisotropic shape and the heterogeneity in the surface chemistry is emphasized in the case of so-called Janus particles, *i.e.* particles with two "faces" having different chemical surface properties,[24,25] many experimental investigations have been focused on their self-assembly at an interface.[26–36]

A pioneering study on the self-assembly of colloids at a fluid–fluid interface was performed by Pieranski.[37] In this work interfacial deformation effects were neglected and a flat interface was assumed. This assumption, often used in literature, is actually only valid in the case of homogeneous spherical

[a] *Soft Condensed Matter, Debye Institute for Nanomaterial Science, Utrecht University, Princetonplein 1, Utrecht 3584 CC, The Netherlands. E-mail: m.dijkstra@uu.nl; Tel: +31 30 253 3270*
[b] *Van't Hoff Laboratory for Physical and Colloidal Chemistry, Debye Institute for Nanomaterial Science, Utrecht University, Padualaan 8, Utrecht 3584 CH, The Netherlands*
[c] *Condensed Matter and Interfaces, Debye Institute for Nanomaterial Science, Utrecht University, Princetonplein 1, Utrecht 3584 CC, The Netherlands*
[d] *Institute for Theoretical Physics, Center for Extreme Matter and Emergent Phenomena, Utrecht University, Princetonplein 5, Utrecht 3584 CC, The Netherlands*

† Electronic supplementary information (ESI) available. See DOI: 10.1039/c8sm02361a

particles in equilibrium. In all other cases, it is equivalent to ignoring the induced interfacial deformation field. Nevertheless, following Pieranski's assumption of a flat interface, several numerical techniques have been employed for calculating the equilibrium configuration of an arbitrarily shaped particle adsorbed at a fluid interface: *e.g.* the triangular tessellation technique (TTT),[38–43] and a hit and miss Monte Carlo method.[26,27,29] In order to take into account deformations of the fluid interface that arise when a particle is adsorbed, various numerical methods exist, like the widely used Surface Evolver program,[44] or a recently introduced simulated annealing method.[45] By using the latter, it has been shown that neglecting interfacial effects can lead to erroneous predictions of the particle orientations while with the inclusion of capillarity, self-assemblies have been predicted in agreement with experimental observations.[45–47]

In this paper we employ the simulated annealing method introduced in ref. 45 to numerically study the equilibrium configuration of a single Janus particle adsorbed at a fluid–fluid interface. Our method takes into account the interfacial deformations so that we can predict the adsorption equilibrium configuration and the resulting induced interfacial deformation field. This last information is then exploited for predicting the capillary interactions between a pair of Janus particles at an interface. We also present experimental results on the synthesis, adsorption and self-assembly of charged Janus dumbbells at a water–decane interface. We compare the experimental results with the numerical ones, finding qualitative agreement.

The paper is organized as follows. In Section II we introduce the numerical method employed for our calculations. In Section III we study the adsorption of a single Janus particle at a fluid–fluid interface, *i.e.* we determine the equilibrium configuration and the resulting interfacial deformations. We then study the capillary pair interaction between two particles at an interface. Finally, in Section IV, we present the experimental results and compare them with the numerical predictions.

II. Numerical method

In this section, we briefly illustrate the numerical method for our calculations. We consider two immiscible, homogeneous, and incompressible fluids separated by a fluid–fluid interface. We assume the fluid–fluid interface as a 2D, possibly curved, surface, with zero thickness. When no particles are adsorbed, the fluid–fluid interface coincides with a plane parallel to $z = 0$, where a Cartesian coordinate system x, y, z has been introduced. At equilibrium, the shape of the fluid–fluid interface is given by the Young–Laplace equation, with Young's law as a boundary condition for the contact angle.[45] The contact angle is the angle formed by the fluid–fluid interface along the three-phase contact line, *i.e.* where the fluid–fluid interface encounters any solid surface. When a Janus particle is adsorbed at the fluid–fluid interface, two different contact angles are formed by the fluid–fluid interface with the surface of the two patches of the particle, denoted here by green and violet patches, respectively,

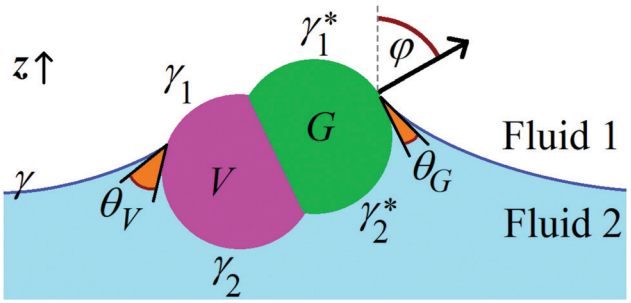

Fig. 1 Sketch of a Janus particle at a fluid–fluid interface. The particle has two patches, indicated in green and violet. The various surface tensions are (see text) γ, γ_1, γ_2, γ_1^*, γ_2^*. The contact angles (measured inside fluid 2) of the fluid–fluid interface with the two patches, respectively θ_G and θ_V are given by Young's Law (see eqn (1)). In our model, the fluid–fluid interface coincides with a plane parallel to $z = 0$ when no particle is adsorbed. The angle φ is the polar angle of the particle vertical axis with respect to the fluid–fluid interface plane with $\varphi = \pi/2$ corresponding to the particle horizontally aligned to the interface, $\varphi = 0$ to the particle vertically aligned and with the green patch upwards, $\varphi = \pi$ to the particle vertically aligned and with the green patch downwards.

in Fig. 1. We call γ the fluid–fluid surface tension between the two fluids, γ_1, γ_2 the surface tensions of the violet patch with fluid 1 and fluid 2, respectively, and γ_1^*, γ_2^* the surface tensions of the green patch with fluid 1 and fluid 2, respectively. By convention, fluid 1 is the fluid at $z \to +\infty$ and fluid 2 the fluid at $z \to -\infty$. From Young's Law,[45] the contact angles θ_V and θ_G, relative to the violet (V) and green (G) patch of the particle as indicated in Fig. 1, are given by

$$\cos\theta_V = \frac{\gamma_1 - \gamma_2}{\gamma}, \quad \cos\theta_G = \frac{\gamma_1^* - \gamma_2^*}{\gamma}, \tag{1}$$

respectively. To study the adsorption of a Janus particle at a fluid–fluid interface, including the effects of capillary deformations, the equilibrium shape of the fluid–fluid interface, with respect to the particle position at the interface, is required. We compute the equilibrium shape using the numerical method introduced in ref. 45. In this method, the fluid–fluid interface is treated as a grid of points, and a simulated annealing algorithm[48] is used to find the point positions that minimize the thermodynamic potential ("energy") of the solid–fluid–fluid system, given the fixed position of the solid surfaces in the system as an input parameter. In our case, the solid surface position is defined by the positions and orientations of the N particles adsorbed at the fluid–fluid interface. We define them by the $5N$-dimensional vector $\Omega = (\Omega_1, \ldots, \Omega_N)$, with $\Omega_i = (x_i, y_i, z_i, \varphi_i, \alpha_i)$ defining the configuration of the i-th particle ($i = 1, \ldots, N$), where x_i, y_i are the in-plane Cartesian coordinates of the center of mass, z_i is the difference between the Cartesian coordinate z of the center of mass and the interface height far away from the particle, φ_i is the polar angle of the vertical axis with respect to the far-field interface normal (see Fig. 1), and α_i is the azimuthal angle of the particle vertical axis in the interface plane. Note that, since we consider particle shapes that are rotational invariant around their long axis, we do not need to specify a third Euler

angle. The energy of the particles–fluid–fluid system can be written as[45]

$$E_N(\Omega) = \gamma(S(\Omega) - A + W_G(\Omega)\cos\theta_G + W_V(\Omega)\cos\theta_V), \quad (2)$$

where $S(\Omega)$ is the total fluid–fluid surface area, $W_G(\Omega)$ and $W_V(\Omega)$ are the total surface areas between fluid 1 and the green and violet patches, respectively. The constant A is the planar fluid–fluid surface area when no particle is adsorbed, and is included in eqn (2) to set the energy level $E_N = 0$ when all particles are desorbed from the interface and are immersed in fluid 2.

For a given set of input parameters θ_G, θ_V and Ω, we compute first the equilibrium shape of the fluid–fluid interface using our numerical method. Once the equilibrium shape is known, we extract the minimum energy E_N for these input parameters. By repeating this procedure for different Ω enables us to find the equilibrium particle configuration that minimizes the total energy of the system as well as the equilibrium shape of the fluid–fluid interface, including the equilibrium position of the three-phase contact line. The resulting contact angles, after the energy is minimized matches the input values θ_G, θ_V used in eqn (2). In order to mimic an infinitely flat interface far away from the particle, we place a solid vertical wall with contact angle $\pi/2$ far away around our particle–fluid–fluid system to avoid particle–wall capillary interaction effects. In all the calculations presented in this work, the fluid–fluid interface shape that minimizes $E_N(\Omega)$ (eqn (2)) is computed allowing fluid 1 and fluid 2 to exchange volume. So the minimum-energy level of the interface far away from the particles, for a given Ω, is automatically found when the equilibrium shape of the interface is computed. More details on the numerical method can be found in ref. 49. Other examples of its application to colloidal particles at fluid–fluid interfaces and for a droplet in contact with heterogeneous surfaces can be found in ref. 46, 47, 50, 51 and 52.

III. Numerical results

In this section, we report our numerical results for the adsorption and capillary interactions of Janus colloidal particles at a fluid–fluid interface. First, the equilibrium orientation of a single adsorbed particle is shown, for different shapes and contact angles of the Janus particle. Then, the interfacial deformations induced by the adsorbed particle are analyzed. Finally, we study the capillary pair interaction between two identical particles adsorbed at the interface. The shapes of the Janus particles considered in this work are shown in Fig. 2: (a) a dumbbell of two spheres of radius R and center-to-center distance d, (b and c) a dumbbell with (b) a short and (c) a long inter-sphere cylindrical neck of radius $R_0 < R$ and length L, and (d) a spherocylinder of cylinder length L and radius $R_0 = R$. The Janus character of all four particles (a–d) is also illustrated in Fig. 2, *i.e.* such that the uniaxial character of the particles is preserved.

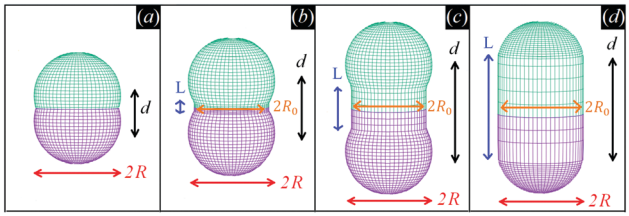

Fig. 2 (a) Janus dumbbell consisting of two interpenetrating spheres with radius R and center-to-center distance $d = \sqrt{2}R$. (b) Janus dumbbell consisting of two interpenetrating spheres with radius R and a small cylindrical part connecting them, with radius $R_0 = R/\sqrt{2}$ and length $L = (1.7 - \sqrt{2})R$,, for d = 1.7R. (c) Janus dumbbell consisting of two touching spheres with radius R and a cylindrical part connecting them, with $R_0 = R/\sqrt{2}$ and $L = (2 - \sqrt{2})R$, for d = 2R. (d) The limiting case of a Janus spherocylinder of two touching spheres of radius R and a cylindrical part of length L with $2R_0 = L = d = 2R$.

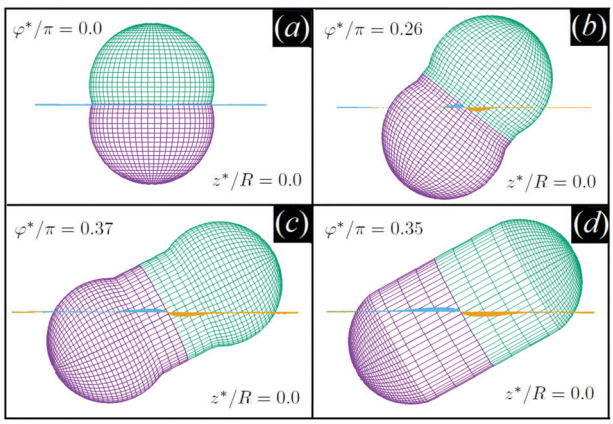

Fig. 3 3D views of the equilibrium configuration of a Janus particle with the shapes shown in Fig. 2 at a fluid–fluid interface, and with contact angles of the green and violet patches (see Fig. 1) given by $\cos\theta_G = -\cos\theta_V = -0.4$. While the equilibrium particle height on the interface level far away from the particle is, as expected, $z^* = 0$, in all cases, the orientation φ^*/π depends on the particle shape. In case (a) $\varphi^*/\pi = 0$, and no interfacial deformations are induced. In cases (b–d), the particle is tilted with respect to the interface and the interfacial deformation field is dominated by a hexapolar mode with increasing intensity upon increasing the length of the cylindrical part of the Janus dumbbell.

A. Single adsorbed particle

Here we present the equilibrium orientation of a single-adsorbed Janus particle, for each of the particle shapes shown in Fig. 2, and for various values of the contact angles θ_G and θ_V of the two particle patches. Next, we analyze the interfacial deformation field induced by each particle when adsorbed in equilibrium.

The configuration of a single-adsorbed particle at the interface, using the notation of Section II, is $\Omega = (x, y, z, \varphi, \alpha)$, where the subscript "1" is omitted since we consider a single particle (*i.e.* $N = 1$). In Fig. 3, we show a 3D view of the equilibrium adsorption configuration of a Janus particle, for the different shapes shown in Fig. 2 and for $\cos\theta_G = -\cos\theta_V = -0.4$. The equilibrium values z^* and φ^* of the particle height z measured with respect to the interface level far away from the particle and

of the particle orientation φ are reported for each shape. Since we consider a single-particle at a planar fluid–fluid interface, x, y, and α of the particle are irrelevant by symmetry. The dumbbell (shape (a) of Fig. 2) prefers the vertically aligned orientation, with the green patch completely immersed in fluid 1 and the violet patch completely immersed in fluid 2. The other three particle shapes, (b–d) of Fig. 2, instead, prefer a tilted orientation, with the green patch predominantly immersed in fluid 1 and the violet patch largely immersed in fluid 2. The equilibrium polar tilt angle φ^* increases monotonically from case (a) to case (d). This is due to the fact that for a longer cylindrical part of the particle, the surface area that is excluded from the fluid–fluid interface increases, when the particle is more tilted. As a consequence, the tilt of the adsorbed particle increases with the length of the cylindrical neck of the particle. For each of the four cases shown in Fig. 3, we report in Fig. 4 a contour plot of the fluid–fluid interface height profile, as computed through our method. The dumbbell in its equilibrium adsorption configuration does not deform the interface, while an asymmetric hexapolar capillary deformation is found in the other three cases, as will be discussed in more detail in the next section.

As the interfacial deformation field is most pronounced for the Janus spherocylinder, we will use this particle shape to investigate the role of the contact angles θ_G and θ_V. In Fig. 5 we show a 3D view of the equilibrium configuration of a spherocylinder (shape (d) of Fig. 2) for $\cos\theta_G = -0.4$, 0, 0.4 and $\cos\theta_V = -0.4$, 0, 0.4. In the graph of Fig. 5, the diagonal cases with $\cos\theta_G = \cos\theta_V$ correspond to the cases of a homogeneous (*i.e.* non-Janus) spherocylinder. The other cases of Fig. 5 are symmetric with respect to this diagonal, with the green and violet patch exchanging role (since their contact angles are interchanged).

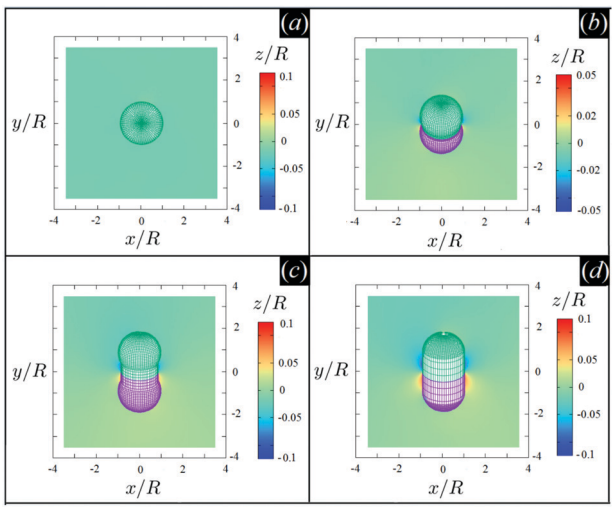

Fig. 4 Contour plots of the interfacial deformation field of the Janus particles adsorbed at a fluid–fluid interface at their equilibrium configurations as shown in Fig. 3. A flat plane corresponds to the shape of the fluid–fluid interface when no particle is adsorbed. In case (a), the particle does not induce any deformation (*i.e.* the interface remains flat). In case (b–d), a hexapolar mode is observed, whose intensity is maximum in the case of the spherocylinder (d). This case is analyzed in detail in Section IIIB.

In the case $\cos\theta_G = \cos\theta_V = 0$, the equilibrium height of the spherocylinder's center of mass at the interface level is $z^* = 0$, the spherocylinder prefers the horizontal orientation, *i.e.* $\varphi^*/\pi = 0.5$, and no interfacial deformations are observed, *i.e.* the interface remains flat also in the presence of the particle. When $\cos\theta_G = \cos\theta_V = \pm 0.4$, the spherocylinder is also horizontal at the interface, but $z^*/R = 0.40$. Note that the equilibrium heights are of the same magnitude, since these cases are symmetric with respect to z (inverting the sign of the cosine of the contact angle is equivalent to exchanging fluid 1 and fluid 2, see eqn (1)). Along the diagonal, where $\theta_G = \theta_V$, the interfacial height profile is flat as expected.[53] In all the off-diagonal cases, the spherocylinder at the equilibrium stays tilted at the interface, *i.e.* $\varphi^*/\pi \neq 0.5$. In particular, the bigger $|\cos\theta_G - \cos\theta_V|$, the more the spherocylinder is tilted. Most interestingly, in all the off-diagonal cases, *i.e.* where the spherocylinder is a Janus particle, the interfacial deformation field is dominated by a hexapolar mode, rather than by a flat interface as observed for the non-Janus spherocylinders. We will discuss this in detail in the next section.

Analogous graphs to Fig. 5 are reported in Fig. S2–S4 in the ESI,† for the other three particle shapes which show that the intensity of the interfacial deformation field decreases upon decreasing the length of the cylindrical part of the Janus dumbbell. Also, in Fig. S1 of the ESI,† we report the energy E_1 (eqn (2)) computed by our numerical method for all particle orientations φ considered, and for all the particle shapes and contact angle values considered. Since we perform calculations for many particle shapes and contact angles we consider a relatively large step size $\Delta\varphi = 0.05\pi$ and a relatively large grid spacing of $0.007R$.

B. Fit of the interfacial deformation field

Within the approximation of small interfacial deformations, the equilibrium height profile of a fluid–fluid interface around a colloidal particle centered in the origin can be written as[6,13]

$$\frac{h(r,\phi)}{R} = C_0 \ln\left(\frac{r}{R}\right) + \sum_{m=1}^{\infty} C_m \frac{\cos(m(\phi-\phi_m))}{(r/R)^m}, \qquad (3)$$

where we introduced the cylindrical coordinates r and ϕ, with $r = \sqrt{x^2+y^2}$ and $\phi = \arctan\left(\frac{y}{x}\right)$, and the fluid–fluid interface far away from the particle is at $z = 0$. In eqn (3), the coefficients C_0, C_m and ϕ_m are referred to, respectively, as the monopole (C_0), the dipole (C_1), the quadrupole (C_2), the hexapole (C_3), *etc.* We consider the case of the Janus spherocylinder with $\cos\theta_G = -\cos\theta_V = 0.4$, as shown in Fig. 3(d) and 4(d). In Fig. 6, we report the height profile $h(r,\phi)/R$ as a function of ϕ for the two distinct values $r/R = 2$ and $r/R = 5$ as computed through our numerical method. The fit shown in the figure is obtained by the multipole expansion eqn (3) with the coefficients as reported in Table 1, and neglecting the modes with $m \geq 4$.

The monopolar and dipolar modes are not expected for a particle at its equilibrium adsorption configuration, unless external forces are applied to the particle.[13] In our case these modes approach zero when a very accurate equilibration of the particle configuration (step size $\Delta\varphi = 0.001\pi$ and grid spacing

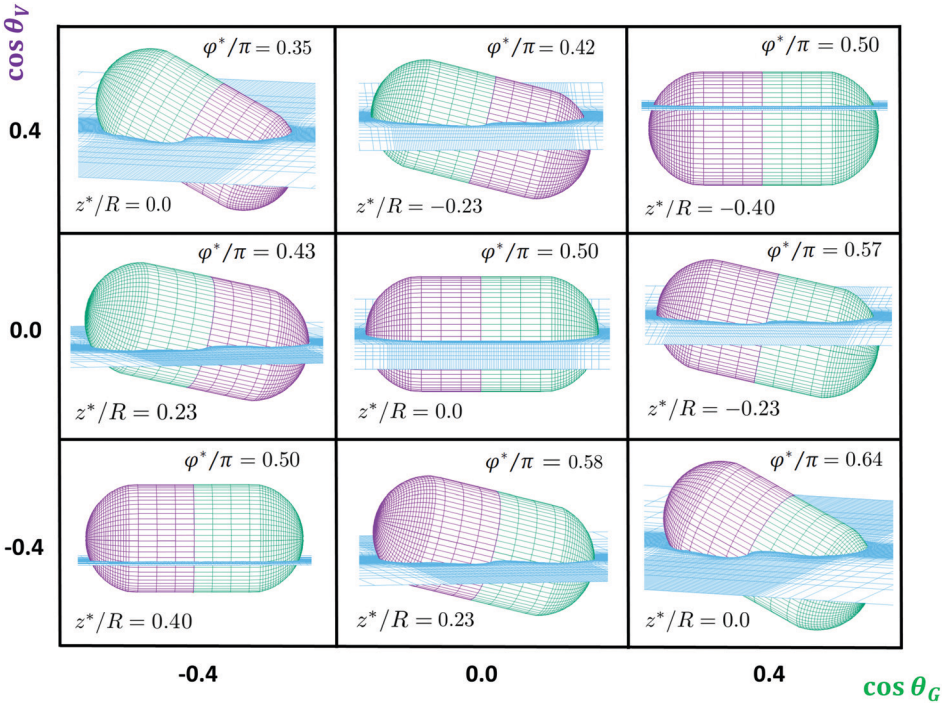

Fig. 5 3D views of the equilibrium configurations of a Janus spherocylinder (shape (d) in Fig. 2) adsorbed at a fluid–fluid interface, with varying contact angles θ_G and θ_V. The graph is symmetric with respect to the diagonal corresponding to the cases of a homogeneous (non-Janus) spherocylinder, *i.e.* $\theta_G = \theta_V$. When $\cos\theta_G = \cos\theta_V = 0$, $\varphi^*/\pi = 0.5$, $z^* = 0$, no interfacial deformations are induced in the fluid–fluid interface shape. For $\cos\theta_G = \cos\theta_V = \pm 0.4$, $\varphi^*/\pi = 0.5$, $z^*/R = 0.40$, the induced interfacial deformation fields are flat as expected.[53] In all the off-diagonal cases, the deformation field is dominated by the hexapolar mode, whose intensity is proportional to $|\cos\theta_G - \cos\theta_V|$. This is shown in detail in Section IIIB.

$0.0001R$) is performed. However, due to the precision of our numerical method these modes never disappear completely. Nevertheless their amplitudes $C_0 \approx -0.00071$ and $C_1 \approx -0.0063$ are much smaller than the one of the hexapolar mode $C_3 \approx -0.069$. Additionally the quadrupolar mode $C_2 \approx -0.0072$ is also much weaker than C_3 and thus the hexapolar mode is the dominant mode. In Fig. 6 the combination of the hexapolar and quadrupolar modes can only be appreciated at small distances ($r/R = 2$), since at large distances ($r/R = 5$) only the lower order terms of eqn (3) survive. The deviation of the fit from the numerically obtained one for small r/R is caused by neglecting high-order modes with $m \geq 4$ in eqn (3).

C. Capillary pair interaction

After showing the equilibrium configuration of a single-adsorbed Janus particle and the induced deformation field, we consider the capillary pair interactions between two identical Janus particles adsorbed at the interface. Following ref. 46, we define the capillary interaction energy per particle as

$$\tilde{E}_N \equiv \frac{E_N}{N} - E_1 \qquad (4)$$

where N is the number of adsorbed particles and E_N is the energy of the fluid–fluid–particles system numerically computed through the method discussed in Section II. Note that $\tilde{E}_N = 0$ when only one particle is adsorbed ($N = 1$), or when N particles are adsorbed, but so far apart that they are not interacting, *i.e.* $E_N = NE_1$. Here we are interested in the pair interaction, $N = 2$. In Fig. 7, we report the interaction energy per particle $\tilde{E}_2$ for two adsorbed Janus spherocylinders with contact angles $\cos\theta_G = -\cos\theta_V = -0.4$, as a function of the distance $D \equiv \sqrt{(x_1 - x_2)^2 + (y_1 - y_2)^2}$ between their centers of mass. The height of the particles at the interface level is $z_1 = z_2 = z^*$, and their orientation is $\varphi_1 = \varphi_2 = \varphi^*$, with z^* and φ^* the equilibrium values found for this particle shape and contact angles (see Section IIIA). The relative azimuthal angle of the two particles in the interface plane is set to $\alpha_1 - \alpha_2 = 0, \pi$, corresponding to a laterally aligned and an anti-aligned configuration, respectively, see Fig. 7. We find attractive capillary interactions for the laterally aligned configuration (black), and repulsive capillary interactions for the anti-aligned configuration (orange). Interestingly, this result is only expected when the dominant mode of the interfacial deformation field induced by the two particles is a hexapole, as in our results. Instead, if the dominant mode had been a quadrupole, attractive capillary interactions would have been found for both laterally aligned and anti-aligned configurations. This is a key finding of this paper that allows us to experimentally distinguish particles with quadrupolar and hexapolar deformation fields, as we will discuss in Section IV. We also mention here that the residual dipolar mode found in the previous paragraph does not significantly affect the pair interaction between the spherocylinders. As shown in Fig. 6, the dipole still survives at a distance $r/R = 5$ from a single

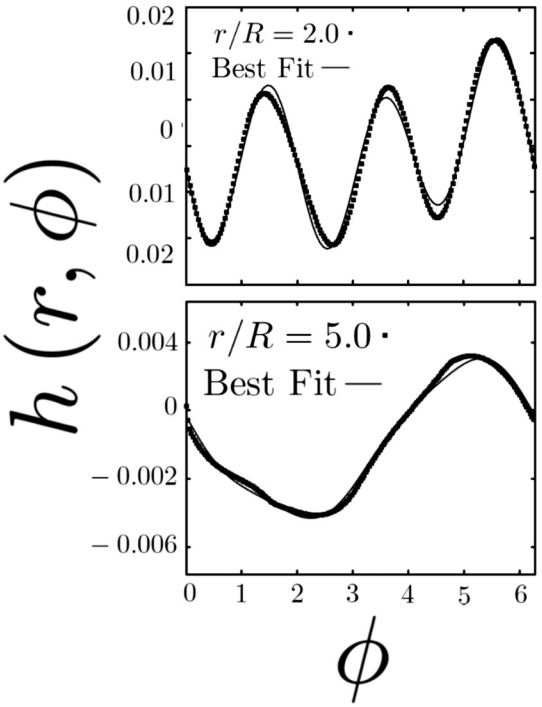

Fig. 6 Interface height profile $h(r,\phi)$ around the Janus spherocylinder at its equilibrium adsorption configuration in the case shown in Fig. 3(d) and 4(d), as a function ϕ, and for the two distinct values of r/R = 2 and r/R = 5, where r and ϕ are cylindrical coordinates (see text). The fit shown in the figure is the multipole expansion eqn (3) with the coefficients as reported in Table 1. The dots represent our numerical solution.

Table 1 Coefficients C_m of the multipole expansion (3) obtained through a fit of the numerical obtained results. Here C_0, C_1, C_2 and C_3 are the amplitudes of the monopolar, dipolar, quadrupolar and hexapolar modes, respectively, while ϕ_1, ϕ_2 and ϕ_3 are their phases

m	$100{\cdot}C_m$	ϕ_m
0	-0.071 ± 0.002	—
1	-0.63 ± 0.03	2.26 ± 0.01
2	-0.72 ± 0.2	0.87 ± 0.23
3	-6.9 ± 1.0	1.26 ± 0.01

spherocylinder while, as shown in Fig. 7, the interaction energy per particle is negligible, if compared to the near contact value, at a distance $D/R \approx 3.6$ between two spherocylinders.

A graph analogous to the one in Fig. 7 is presented in Fig. S5–S7 of the ESI,† for the tip–tip interactions. In this case, within the precision of our numerical method, we do not observe any interaction between the spherocylinders.

Note that the pair potential $\tilde{E}_2$ in Fig. 7 is plotted in units of $\gamma\Sigma$, where Σ is the total surface area of a spherocylinder. For typical values $\gamma \sim 10^{-2}$ N m and micrometer-sized areas $\Sigma \sim 10^{-12}$ m^2, we have $\gamma\Sigma \sim 10^{-14}$ $J \sim 10^7 k_B T$, such that the capillary pair interaction at contact, $\tilde{E}_2 \sim (10^{-4}$–$10^{-3})\gamma\Sigma$ in Fig. 7 corresponds to strong capillary interactions of hundreds of $k_B T$.

We consider the case of a Janus spherocylinder here as the numerical result is the most accurate for this particle shape due

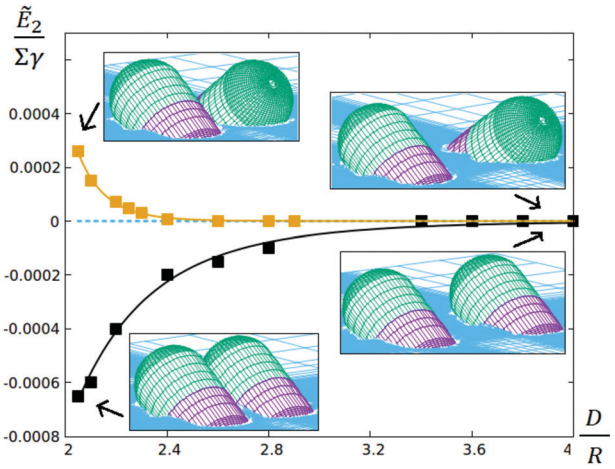

Fig. 7 Interaction energy per particle $\tilde{E}_2/\Sigma\gamma$ (eqn (4)) of two parallel Janus spherocylinders, adsorbed in their equilibrium configuration, as a function of the distance D between their centers of mass, for laterally aligned (black) and anti-aligned (orange) orientations. The total surface area is denoted as Σ and the fluid–fluid surface tension is γ. The contact angles of the Janus spherocylinders are given by $\cos\theta_G = -0.4$ (in green) and $\cos\theta_V = 0.4$ (in violet).

to the high intensity of the interfacial deformation field. We expect similar, but weaker, capillary interactions for the other particle shapes of Fig. 2(b and c) as the deformation fields are qualitatively similar but less pronounced.

IV. Experimental results

In this section we present experimental observations on the adsorption and self-assembly of charged Janus dumbbells at a water–decane interface. We also report some details of the synthesis of the dumbbells and a comparison with the theoretical predictions of the previous sections.

A. Preparation of smooth Janus dumbbells

We prepared linear polystyrene spheres (PS) *via* a soap-free dispersion polymerization. An amount of 90 mg AIBN (Argos Organics) was dissolved in a mixture of 40 mL methanol and 8 mL styrene (St, Sigma-Aldrich) in a 250 mL round bottle flask. Then an aqueous solution of 10 mL H_2O with 130 mg sodium 4-vinylbenzenesulfonate (NaSS) (Aldrich) was added. The flask was flushed with N_2 for 30 minutes and sealed tightly with a stopper and Teflon tape. Polymerization was carried out by placing the flask in an oil bath of 70 °C for 20 hours under magnetic stirring.

The dumbbells were then prepared in two steps (see Fig. 8). This procedure is a modified version of the synthesis described in ref. 54. 3-(Trimethoxysilyl)propylacrylate (TMSPA) was used as comonomer to prepare functional core–shell spheres with a functional shell for further modification. First, PS/poly(St-*co*-TMSPA) core–shell particles were prepared using dispersion polymerization. Typically, a monomer mixture consisting of styrene with 10 v/v% co-monomer 3-(trimethoxysilyl)propylacrylate (TMSPA) (Alfa Aesar, 94%) and 1.5 wt% azobisisobytyronitrile

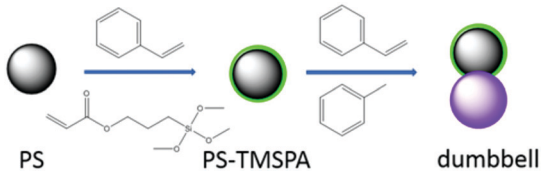

Fig. 8 Schematic illustration of the formation of dumbbells *via* a two-step dispersion modification. More details on the synthesis can be found in Fig. S8 of the ESI.†

(AIBN) was prepared. Then a swelling emulsion was prepared by adding a monomer mixture to the particle seed dispersion (5 wt%). The volume ratio of $V_{monomers}/V_{PS}$ was fixed at 1. After swelling for 20 hours on a roller table at 60 rpm, the polymerization was conducted at 70 °C in an oil bath. The core–shell particles with uniform spherical shape were used as seed particles for the second dispersion polymerization.

In the second step, we mixed 10 mL of the core–shell suspension (5 wt%) with a mixture of styrene, toluene (5 vol% to the styrene) and AIBN (1 wt%) in a 40 mL glass vial, the swelling ratio $V_{monomers}/V_{core-shell}$ was varied to get anisotropic particles. The second swelling process was allowed for 4 hours on a roller table, followed by polymerization at 70 °C. Like the PS spheres, the particles were stabilized by adding NaSS (1 wt/vol% to the polystyrene) to bring charges to the surface of the protrusion. At swelling ratio 2, the resulting particles are symmetric dumbbells (see Fig. 10(a)), while at swelling ratio 1.5, slightly asymmetric dumbbells with a relatively small protrusion lobe could be prepared. These (Fig. 10(b)) were also synthesized and analyzed as we will see in the following. The chemical asymmetry of our dumbbells was confirmed by labelling the seeded lobe with (3-aminopropyl)triethoxysilane-fluorescein isothiocyanate (APS-FITC) *via* silane coupling reaction. Methoxysilane groups on the surface of the seeded lobe of the dumbbells could be further modified to be hydrophobic or hydrophilic to change the equilibrium particle configuration at a liquid–liquid interface. See for more details Fig. S10 of the ESI.†

Compared to the anisotropic particles with a rough seeded lobe from the seeded swelling–shrinking process,[55] both lobes of the particles prepared using our strategy feature a smooth surface due to the linear core–shell seed particles, which is crucial for the interface experiments. The particles were then spread onto the water–decane interface following a procedure described in Fig. S11 of the ESI.†

B. Structure evolution

After the particles were spread onto the water–decane interface, the structural time evolution of the monolayer was monitored with optical microscopy. Fig. 9(a) depicts the initial configuration of the microstructure. The charged dumbbells at the interface give rise to an ordered crystalline monolayer with a few aggregates present, similar to the well-known behavior observed by Pieranski for charged spheres.[37] This is attributed to the dipole–dipole repulsions from the charges on both lobes of the dumbbells. Our particles assemble predominantly by connecting their waists, thereby forming lateral structures (see Fig. 9(b)). Only a few tip–tip configurations were observed which are mainly due to the roughness of the seed lobes during the seeded dispersion polymerization process. The linear chains grow in time until they encounter each other to form interconnected aggregates and branched structures as shown in Fig. 9(c). Because of the presence of electrostatic interaction, the structural evolution proceeds relatively slowly. Fig. 9(d) shows a network structure consisting of rigid linear segments,

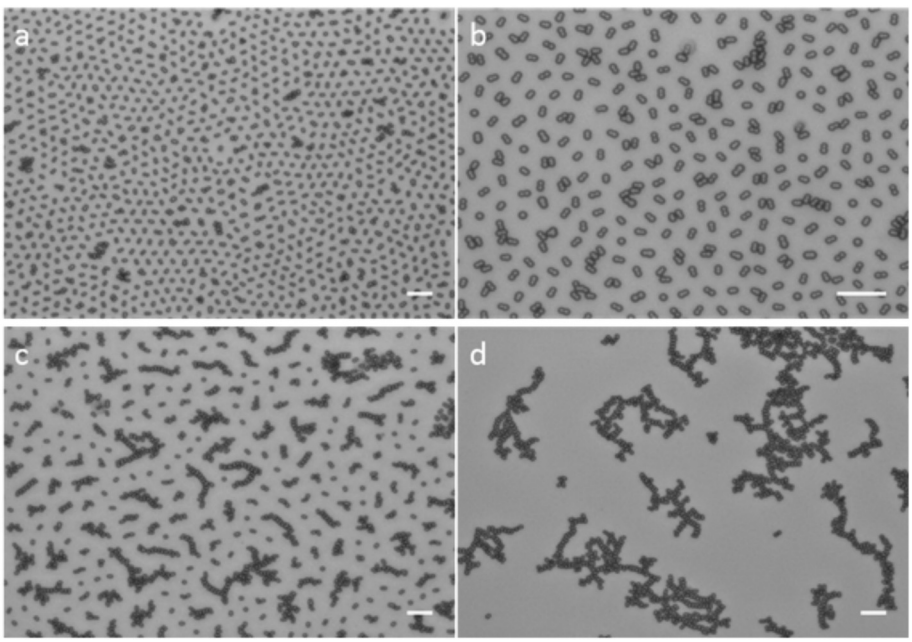

Fig. 9 The structure evolution in a monolayer containing charged Janus dumbbells at the water–decane interface: (a) microstructure obtained right after spreading particles at the interface; after (b) 25 hours; (c) 50 hours; (d) 120 hours. The scale bar corresponds to 20 μm.

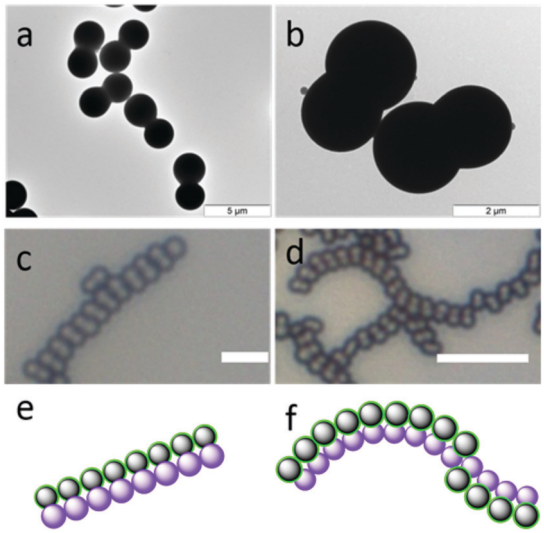

Fig. 10 Transmission electron microscope images of symmetric Janus dumbbells (a) and slightly asymmetric Janus dumbbells (b); a linear string of symmetric Janus dumbbells (c) and a curved chain of slightly asymmetric Janus dumbbells (d) formed at an interface. In case (c and d) the scale bar corresponds to 10 μm. Schematic images of the observed structures: a linear string of laterally aligned symmetric Janus dumbbells (e), a curved chain of laterally aligned and slightly asymmetric Janus dumbbells (f).

and this system evolved to such a state in about 120 hours after spreading. A zoomed image of the observed lateral structures is shown in Fig. 10(c).

Fig. 9 also shows that the particles first form doublets and only at a later stage longer chains, which is expected for charged particles.

C. Discussion and comparison with theoretical predictions

Even if electrostatic forces are present in our system, capillarity is still expected to play a major role in the self-assembly process as was also observed in ref. 56. Therefore a qualitative comparison between our experimental analysis and the numerical predictions should be justified.

As shown in Fig. S9 of the ESI,† the shape of our experimentally synthesized dumbbells can best be compared to the dumbbells of Fig. 2(b and c), rather than to the ones of Fig. 2(c), *i.e.* dumbbells consist of smoothly joined, interpenetrating or touching spheres.

The structures experimentally observed can be explained by an induced deformation field dominated by a hexapolar mode, as predicted by our numerical calculations. Indeed the lateral aggregates that we experimentally observe consist of only laterally aligned configurations of two neighboring particles and never of laterally anti-aligned configurations. Actually this conclusion cannot be inferred from the analysis performed on the symmetric Janus dumbbells. In this case it is impossible to distinguish which lobe of the dumbbell is hydrophilic and which one is hydrophobic so that even if lateral structures are observed, it is not possible to say if they consist of laterally aligned configurations or of laterally anti-aligned ones. It then follows that it is not possible to distinguish between a hexapolar induced capillary deformation field and a quadrupolar one. To clarify this point, slightly asymmetric dumbbells (see Fig. 10(b)) were used as reference. In the case of asymmetric dumbbells, it is possible to distinguish the hydrophobic lobe of the dumbbell from the hydrophilic one since one lobe is slightly bigger than the other. As shown in Fig. 10(d), asymmetric dumbbells evolve into curved chains in which the ''big'' lobe of each particle attracts the ''big'' lobe of the neighboring particle. The same of course happens between the ''small'' lobes. This indicates that the chains consist of laterally aligned configurations and since the dumbbells are just slightly asymmetric, we expect this to also hold for less asymmetric and even symmetric dumbbells. A sketch of the structures observed in these two cases is depicted in Fig. 10(e and f). As explained in Section IIIC, this finding allows us to conclude that the capillary deformation field is hexapolar, in agreement with our numerical predictions.

V. Conclusions

In this paper, we numerically studied the adsorption and the self-assembly at a fluid–fluid interface of a variety of anisotropic Janus particles interpolating between a pair of interpenetrating equal-sized spheres to a spherocylinder by the insertion of a cylindrical neck. Each particle shape has two distinct ''faces'' with contact angles θ_G and θ_V, respectively. Our study was performed using a numerical method that takes into account the interfacial deformations. For (Janus or non-Janus) dumbbells consisting of interpenetrating spheres, we always find a flat interface. For dumbbells with a cylindrical neck and for spherocylinders, we find a flat interface in the non-Janus case ($\cos\theta_G = \cos\theta_V$), and that the deformation field is dominated by an hexapolar mode in the Janus case ($\cos\theta_G \neq \cos\theta_V$). The intensity of this hexapole is proportional to the dimension of the cylindrical neck between the spheres composing the particles and to the difference between their contact angles. The intensity of the hexapole is hence strongest in the case of Janus spherocylinders when $|\cos\theta_G - \cos\theta_V|$ is maximum. We then found that the hexapolar field induces capillary attractions between two laterally aligned Janus spherocylinders at the interface and repulsions for two laterally anti-aligned ones. For micrometer-sized spherocylinders this attraction is of the order of hundreds k_BT and since the other particle shapes are expected to induce qualitatively the same deformation field, we expect qualitatively the same capillary interactions, although a bit weaker. We also synthesized micrometer-sized charged Janus dumbbells and experimentally studied their adsorption and self-assembly at a water–decane interface. We found that interactions that appear to be predominantly capillary in nature act among the particles and lead to the formation of structures of laterally aligned Janus dumbbells. This behavior can be qualitatively explained with our numerical predictions. We will leave a more detailed study on the interplay between electrostatic and capillary interactions and a more quantitative analysis of the deformation field induced by experimentally synthesized Janus dumbbells to future work.

Conflicts of interest

There are no conflicts to declare.

Acknowledgements

The authors acknowledge financial support by the "Nederlandse Organisatie voor Wetenschappelijk Onderzoek" (NWO) TOPPUNT. This work is part of the D-ITP consortium, a program of the NWO that is funded by the Dutch Ministry of Education, Culture and Science (OCW).

Notes and references

1 W. Ramsden, *Proc. R. Soc. London*, 1903, **72**, 156–164.
2 S. U. Pickering, *J. Chem. Soc.*, 1907, **91**, 2001–2021.
3 F. Bresme and M. Oettel, *J. Phys.: Condens. Matter*, 2007, **19**, 413101.
4 P. G. de Gennes, *Rev. Mod. Phys.*, 1985, **57**, 827–863.
5 D. Vella and L. Mahadevan, *Am. J. Phys.*, 2005, **73**, 817–825.
6 D. Y. C. Chan, J. D. Henry and L. R. White, *J. Colloid Interface Sci.*, 1981, **79**, 410–418.
7 E. P. Lewandowski, P. C. Searson and K. J. Stebe, *J. Phys. Chem. B*, 2006, **110**, 4283–4290.
8 D. Ershov, J. Sprakel, J. Appel, M. A. Cohen Stuart and J. van der Gucht, *Proc. Natl. Acad. Sci. U. S. A.*, 2013, **110**, 9220–9224.
9 R. Di Leonardo, F. Saglimbeni and G. Ruocco, *Phys. Rev. Lett.*, 2008, **100**, 106103.
10 J. N. Israelachvili, *Intermolecular and surface forces/Jacob N. Israelachvili*, Academic Press London, San Diego, 2nd edn, 1991, p. xxi, 450.
11 N. Bowden, A. Terfort, J. Carbeck and G. M. Whitesides, *Science*, 1997, **276**, 233–235.
12 J. C. Loudet, A. M. Alsayed, J. Zhang and A. G. Yodh, *Phys. Rev. Lett.*, 2005, **94**, 18301.
13 D. Stamou, C. Duschl and D. Johannsmann, *Phys. Rev. E: Stat. Phys., Plasmas, Fluids, Relat. Interdiscip. Top.*, 2000, **62**, 5263–5272.
14 S. Coertjens, P. Moldenaers, J. Vermant and L. Isa, *Langmuir*, 2014, **30**, 4289–4300.
15 M. Zanini and L. Isa, *J. Phys.: Condens. Matter*, 2016, **28**, 313002.
16 J. C. Loudet and B. Pouligny, *Eur. Phys. J. E: Soft Matter Biol. Phys.*, 2011, **34**, 76.
17 G. Morris, K. Hadler and J. Cilliers, *Curr. Opin. Colloid Interface Sci.*, 2015, **20**, 98–104.
18 N. Sharifi-Mood, I. B. Liu and K. J. Stebe, *Soft Matter Self-Assembly*, 2016, **193**, 165.
19 T. G. Anjali and M. G. Basavaraj, *Langmuir*, 2017, **33**, 791–801.
20 M. Cavallaro, L. Botto, E. P. Lewandowski, M. Wang and K. J. Stebe, *Proc. Natl. Acad. Sci. U. S. A.*, 2011, **108**, 20923–20928.
21 S. Dasgupta, T. Auth and G. Gompper, *J. Phys.: Condens. Matter*, 2017, **29**, 373003.
22 E. P. Lewandowski, M. Cavallaro, L. Botto, J. C. Bernate, V. Garbin and K. J. Stebe, *Langmuir*, 2010, **26**, 15142–15154.
23 E. P. Lewandowski, J. A. Bernate, A. Tseng, P. C. Searson and K. J. Stebe, *Soft Matter*, 2009, **5**, 886–890.
24 P. G. de Gennes, *Rev. Mod. Phys.*, 1992, **64**, 645–648.
25 C. Casagrande, P. Fabre, E. Raphaël and M. Veyssié, *Europhys. Lett.*, 1989, **9**, 251–255.
26 B. J. Park and D. Lee, *Soft Matter*, 2012, **8**, 7690–7698.
27 B. J. Park and D. Lee, *ACS Nano*, 2012, **6**, 782–790.
28 A. Kumar, B. J. Park, F. Tu and D. Lee, *Soft Matter*, 2013, **9**, 6604–6617.
29 B. J. Park, C.-H. Choi, S.-M. Kang, K. E. Tettey, C.-S. Lee and D. Lee, *Langmuir*, 2013, **29**, 1841–1849.
30 D. W. Kang, W. Ko, B. Lee and B. J. Park, *Materials*, 2016, **9**, 664.
31 L. Isa, N. Samudrala and E. R. Dufresne, *Langmuir*, 2014, **30**, 5057–5063.
32 K.-H. Roh, D. C. Martin and J. Lahann, *Nat. Mater.*, 2005, **4**, 759.
33 J.-W. Kim, R. J. Larsen and D. A. Weitz, *J. Am. Chem. Soc.*, 2006, **128**, 14374–14377.
34 J.-W. Kim, D. Lee, H. C. Shum and D. A. Weitz, *Adv. Mater.*, 2008, **20**, 3239–3243.
35 L. C. Bradley, W.-H. Chen, K. J. Stebe and D. Lee, *Curr. Opin. Colloid Interface Sci.*, 2017, **30**, 25–33.
36 Q. Xie, G. B. Davies and J. Harting, *ACS Nano*, 2017, **11**, 11232–11239.
37 P. Pieranski, *Phys. Rev. Lett.*, 1980, **45**, 569–572.
38 J. de Graaf, M. Dijkstra and R. van Roij, *Phys. Rev. E: Stat., Nonlinear, Soft Matter Phys.*, 2009, **80**, 51405.
39 J. de Graaf, M. Dijkstra and R. van Roij, *J. Chem. Phys.*, 2010, **132**, 164902.
40 A. R. Morgan, N. Ballard, L. A. Rochford, G. Nurumbetov, T. S. Skelhon and S. A. F. Bon, *Soft Matter*, 2013, **9**, 487–491.
41 W. van der Stam, A. P. Gantapara, Q. A. Akkerman, G. Soligno, J. D. Meeldijk, R. van Roij, M. Dijkstra and C. de Mello Donega, *Nano Lett.*, 2014, **14**, 1032–1037.
42 B. Peng, G. Soligno, M. Kamp, B. de Nijs, J. de Graaf, M. Dijkstra, R. van Roij, A. van Blaaderen and A. Imhof, *Soft Matter*, 2014, **10**, 9644–9650.
43 N. Ballard and S. A. F. Bon, *J. Colloid Interface Sci.*, 2015, **448**, 533–544.
44 K. A. Brakke, *Exper. Math.*, 1992, **1**, 141–165.
45 G. Soligno, M. Dijkstra and R. van Roij, *J. Chem. Phys.*, 2014, **141**, 244702.
46 G. Soligno, M. Dijkstra and R. van Roij, *Phys. Rev. Lett.*, 2016, **116**, 258001.
47 G. Soligno, M. Dijkstra and R. Van Roij, *Soft Matter*, 2017, **14**, 42–60.
48 S. Kirkpatrick, C. D. Gelatt and M. P. Vecchi, *Science*, 1983, **220**, 671–680.
49 G. Soligno, *Droplets, capillary interactions and self-assembly from the equilibrium shape of fluid-fluid interfaced*, PhD thesis, Utrecht University, 2017.
50 M. Vis, J. Opdam, I. S. J. van't Oor, G. Soligno, R. van Roij, R. H. Tromp and B. H. Erné, *ACS Macro Lett.*, 2015, **4**, 965–968.
51 I. Dević, G. Soligno, M. Dijkstra, R. van Roij, X. Zhang and D. Lohse, *Langmuir*, 2017, **33**, 2744–2749.

52 M. Kamp, G. Soligno, F. Hagemans, B. Peng, A. Imhof, R. van Roij and A. van Blaaderen, *J. Phys. Chem. C*, 2017, **121**, 19989–19998.
53 T. G. Anjali and M. G. Basavaraj, *J. Colloid Interface Sci.*, 2016, **478**, 63–71.
54 J.-G. Park, J. D. Förster and E. R. Dufresne, *J. Am. Chem. Soc.*, 2010, **132**, 5960–5961.
55 D. J. Kraft, R. Ni, F. Smallenburg, M. Hermes, K. Yoon, D. A. Weitz, A. van Blaaderen, J. Groenewold, M. Dijkstra and W. K. Kegel, *Proc. Natl. Acad. Sci. U. S. A.*, 2012, **109**, 10787–10792.
56 B. Madivala, J. Fransaer and J. Vermant, *Langmuir*, 2009, **25**, 2718–2728.